

Supporting Information for “*On the theory of the divergence method for quantifying source emissions from satellite observations*”

E. F. M. Koene¹, D. Brunner¹ & G. Kuhlmann¹

¹Empa, Swiss Federal Laboratories for Materials Science and Technology, Überlandstrasse 129, Dübendorf, Switzerland

Contents of this file

1. Examples S1 to S8
2. Figure S1 to S3
3. Text S1 and S2

Examples S1 to S8.

We provide a set of 8 simple 1D examples that illustrate the ‘topography correction’ term (perhaps better-called the ‘topography *gradient* correction’ term) and ‘wind divergence correction’. They do not follow from the theory of mass conservation, but can be useful when a specific type of error is made in areas with topography or areas with considerable wind divergence.

Figure S1 to S3.

We illustrate the effect that operators D_0 , D_1 and D_2 as introduced in the main text have on the SMARTCARB dataset in Figure S1, a synthetic set of CO₂ columns that mimics the CO2M mission characteristics (Kuhlmann et al., 2020). We use a full year of synthetic column and wind data from a constellation of three satellites. The wind field was vertically weighted to the GNFR-A emission profile, corresponding to typical power plant emission profiles (Brunner et al., 2019). Supplementary Figure S2 repeats the analysis with ERA-5 100 m wind data. We compute the divergence operations for each overpass, and then bin the results on a regular $0.03^\circ \times 0.03^\circ$ grid. We compute the operators for both the TVCD (thus it has a background of about 400 ppm) and the EVCD which has the median value of the image subtracted (thus it has a background of about 0 ppm). The value X in D_2 was optimized for every 15×15 pixel region in the image in terms of minimizing the mean squared value.

Figure S1 shows the flux maps. Rows S1(a) and S1(b) show that D_0 applied to the TVCD yields extreme values, while this is alleviated with the EVCD. Column S1(c) shows that similar results are obtained with D_1 , and finally column S1(d) shows how the topographical imprint is reduced with the added surface topography term.

A possible reason for the advantageous effects may be gathered from Figure S3, which shows that the topography correction term is an effective *substitute* for the wind divergence term. In other words, D_2 is a better way to compute D_0 if we do not use the appropriate effective winds.

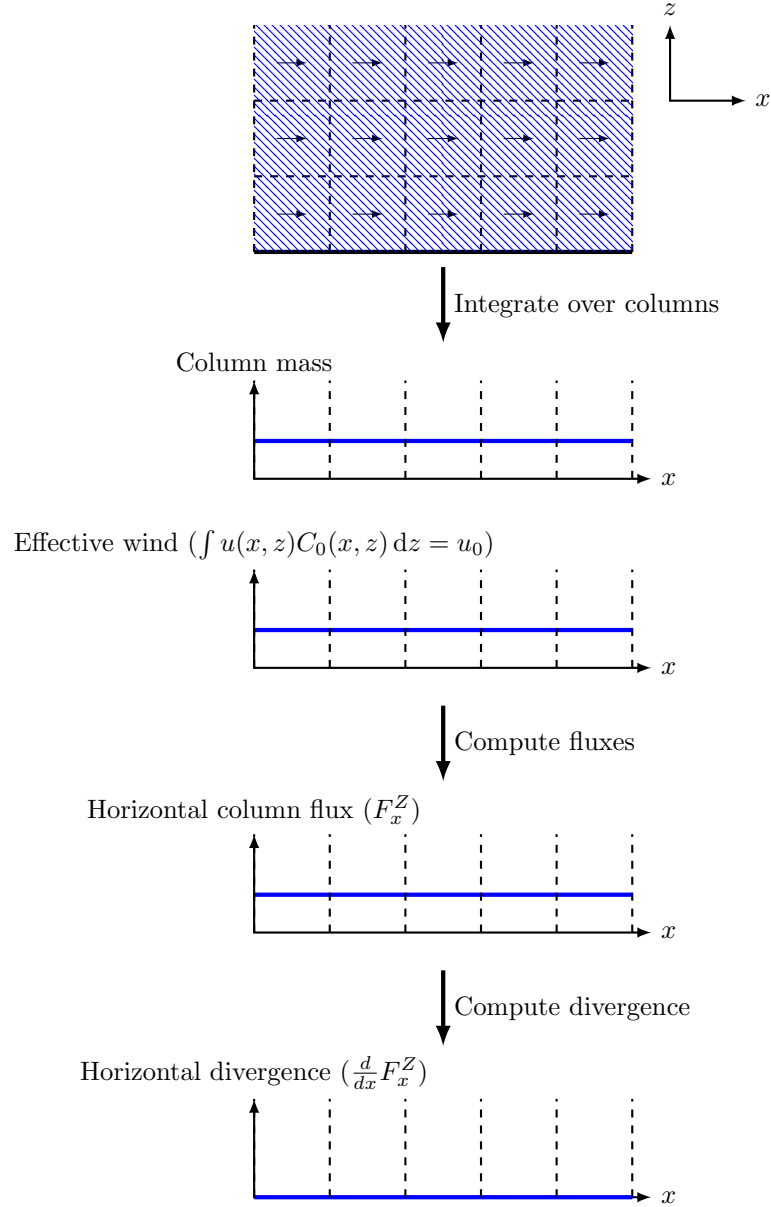
We do not see a verification for the arguments of Sun (2022) who derives that the improvement of using D_1 is needed for correcting air exchange through the top of the column, because the SMARTCARB dataset and the COSMO-GHG dataset consist of total columns – in other words, if using D_1 instead of D_0 has an effect on our dataset, it is not because it corrects for air exchange through the top of the column. Indeed, while $\nabla \cdot [u \ v \ w]^T = 0$ is a valid assumption for incompressible advective flow, it does not immediately follow that $\nabla_{x,y} \cdot [U_Z \ V_Z]^T = 0$ if there are vertical winds and if one computes the effective wind from only a few levels near the surface – Supplementary Information Examples S1–S8 show various examples of effective wind speeds varying in space in valid ways. As remarked above, a more likely reason for the advantageous effects of D_1 (i.e., removing the wind divergence term) is that it paves the road for adding the topography correction term back in (which, we show, is an approximation of the wind divergence term).

Indeed, when looking at Figure S1 we see that S1(d) using operator D_2 removes errors due to the topography that were visible in Figure S1(b) and S1(c); a fix also seen in Figure S3. The reason we give for this improvement is because the effective wind should vary with the topography (terrain-forced flows, for example, force wind speeds to be higher over a hill than its surroundings; while valleys are protected from high wind speeds) but our chosen effective wind speeds will usually not capture these features appropriately.

Text S1 and S2.

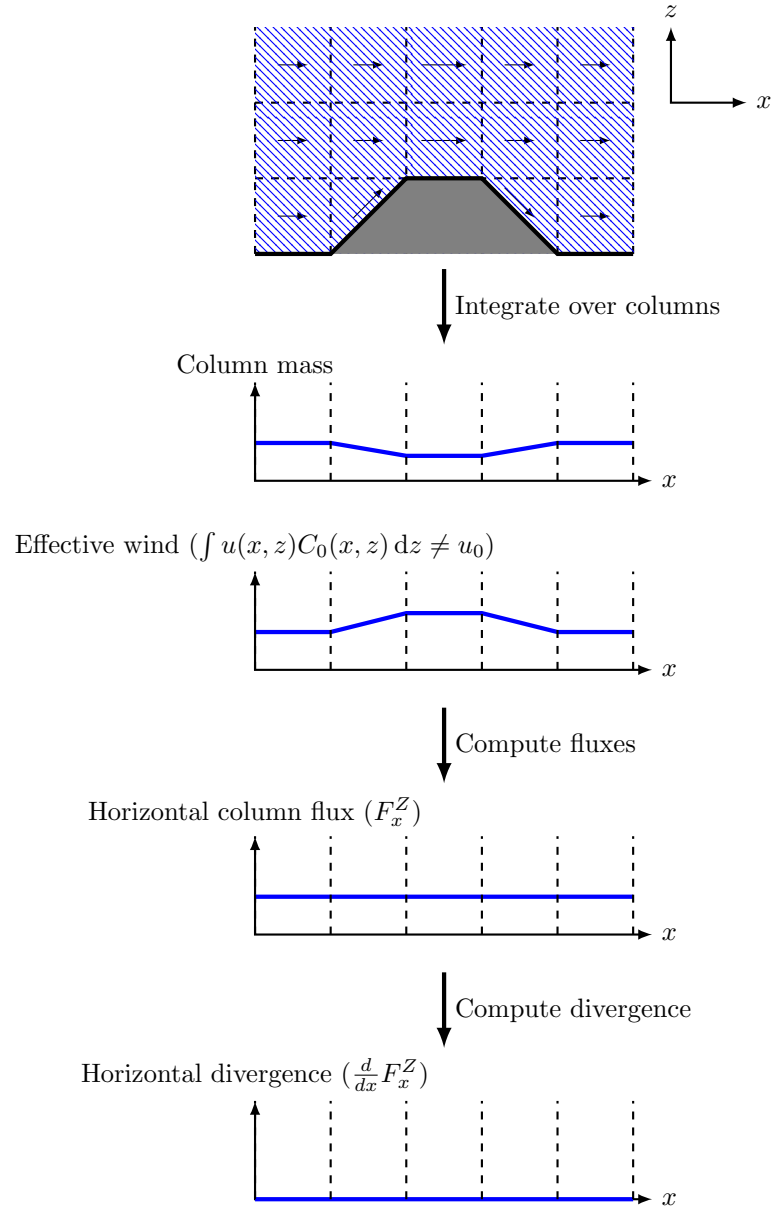
In text S1 we derive the theory of the paper in spherical coordinates rather than Cartesian coordinates – seeing that they lead to equivalent systems. Finally, in text S2 we provide a illustrate that cross-sectional integrals of Gaussian plumes compute the correct source flux as long as the integral is taken along a straight line perpendicular to the wind.

Example S1. Consider the following case where air parcels (drawn as blue hatched boxes enclosed by dashed lines) move over the ground (denoted with the solid black line) with constant horizontal transport speeds $u = u_0$ (denoted with arrows). These are steady-state and source-free conditions.



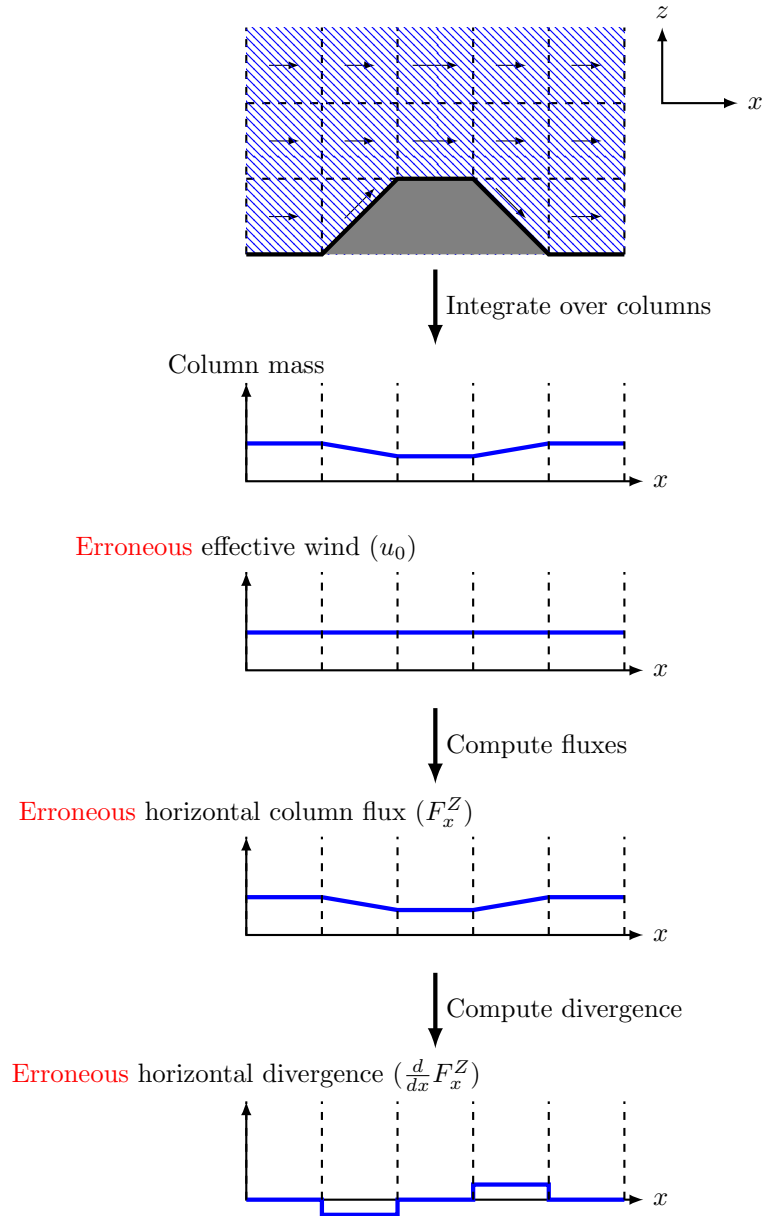
As expected, the horizontal flux field is constant. Thus, the divergence is zero, which is in correspondence with the steady-state source-free state described in this example.

Example S2. We now consider the case where air flows over an idealized hill – while retaining steady-state and source-free conditions. The wind speed along the flanks increases (thus with a considerable non-zero vertical mass flux F_z at the surface) and is maximum on the top of the hill. Note that the wind speed thus is *not* constant.



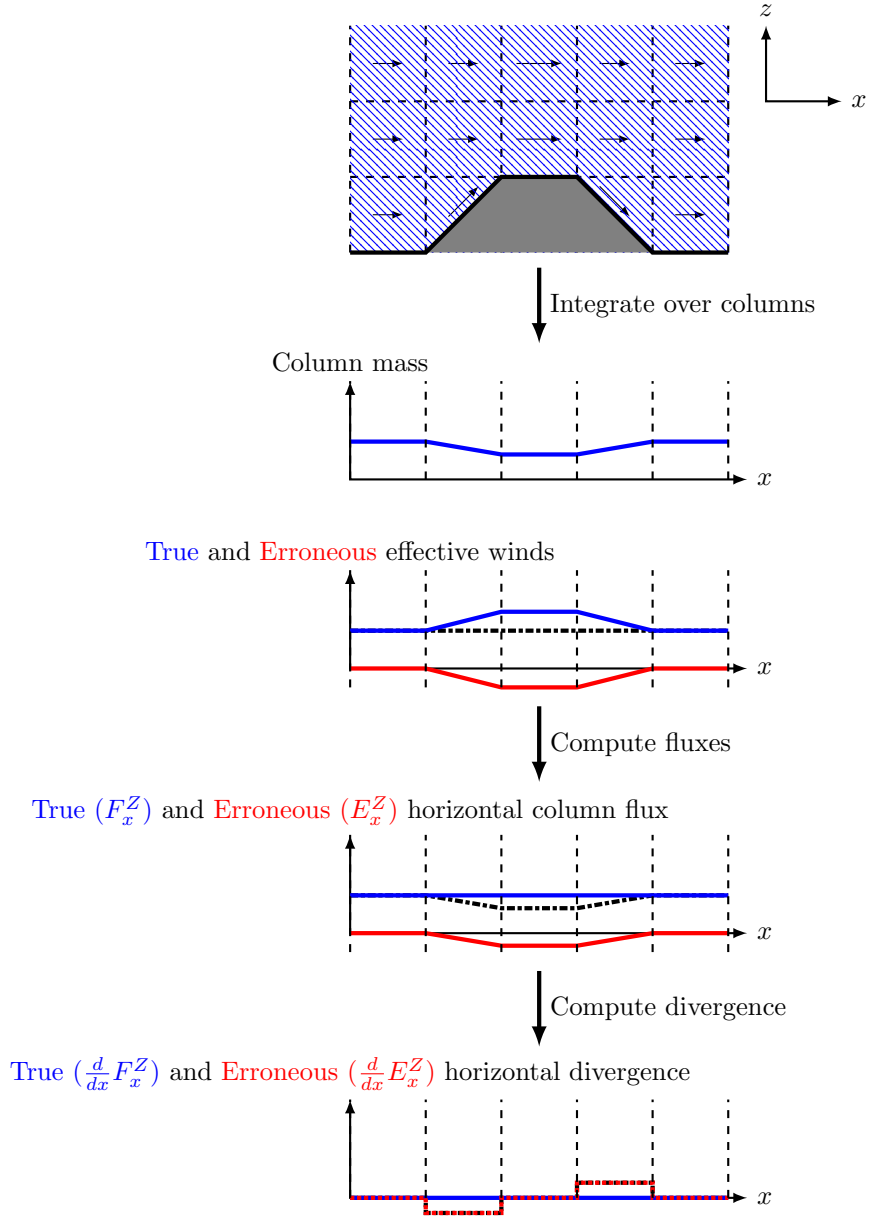
The presence of the hill creates an effective dip in the column mass that is counteracted by the *effective* wind, such that the horizontal column flux remains constant (NB: this is akin to Bernoulli's principle, and is *what is required* for mass conservation). Thus, the divergence of the horizontal column flux is zero, consistent with the source-free steady-state conditions looked at here.

Example S3. We now modify our example such that we use the *erroneous* effective wind instead of the true effective wind.



Use of the erroneous effective wind (for this case) generates a ‘virtual’ source and sink term on the *flanks of the hill*, showing that the error is proportional to the negative gradient of the topography.

Example S4. We now decompose the errors seen in examples S3 into their ‘true’ (cf. example S2) and ‘erroneous’ components, while in black dash-dotted lines we show their net result.

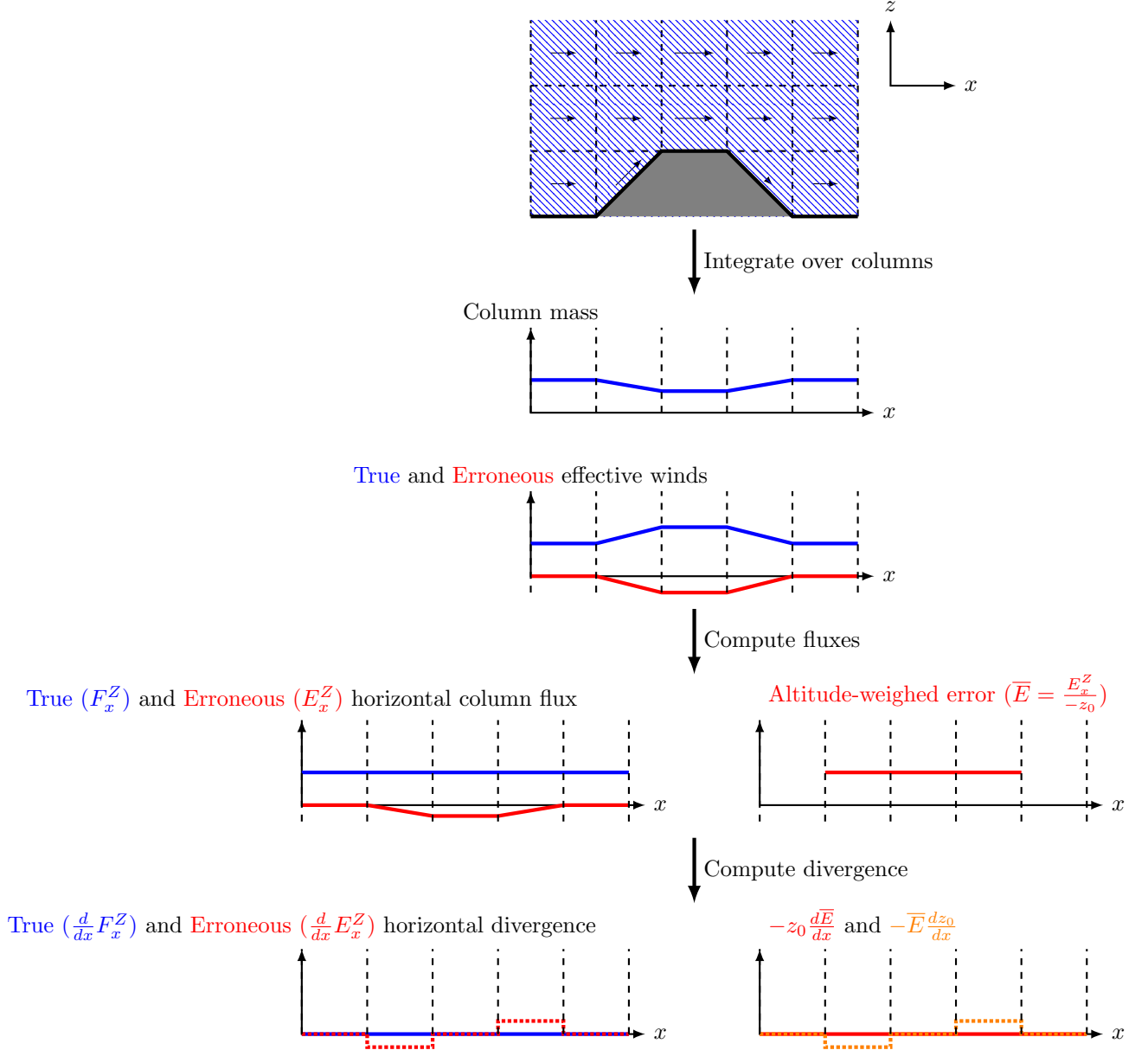


We can thus see that the erroneous effective wind field is negatively correlated with the topography; just like the erroneous horizontal column flux is negatively correlated with the topography. Thus we can observe

$$\frac{d}{dx} E_x^Z = -a \frac{dz_0}{dx}, \quad (\text{S1})$$

for some constant a . We can make this slightly more precise in the next example S5.

Example S5. We now decompose the errors seen in example S4 into topography (or altitude-)weighed quantities: $\bar{E} = E_x^Z / (-z_0)$, such that $dE_x^Z/dx = -\bar{E}(dz_0/dx) - (d\bar{E}/dx)z_0$.

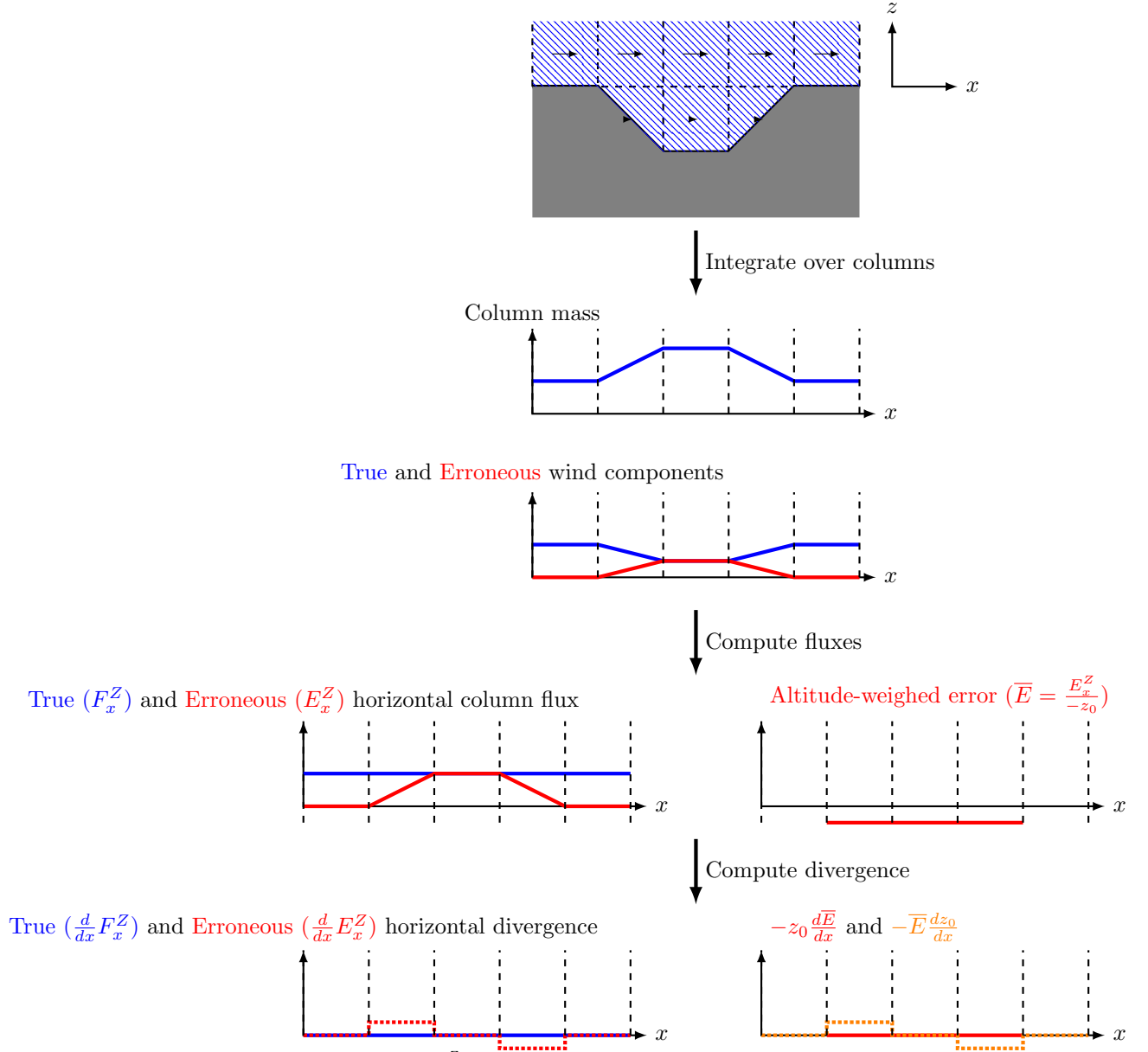


After realizing that $d\bar{E}/dx = 0$, it is now plain to see that the constant a sought under example S4 is exactly the altitude-weighted flux error, \bar{E} , such that we find

$$\frac{d}{dx} E_x^Z = -\bar{E} \frac{dz_0}{dx}. \quad (\text{S2})$$

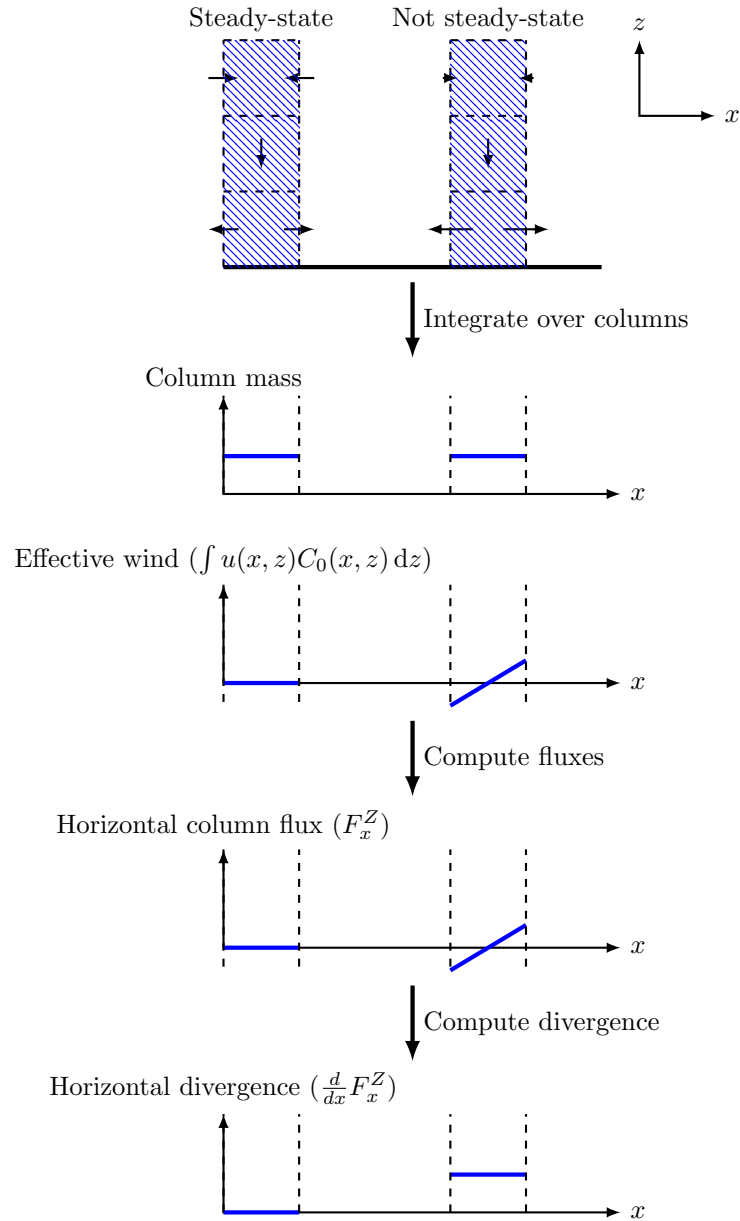
In other words, we can correct for the error made in assuming a constant wind speed (despite the topography) by including a factor proportional to the topography instead.

Example S6. We can invert the situation and also consider a valley case, where the same conclusion holds:



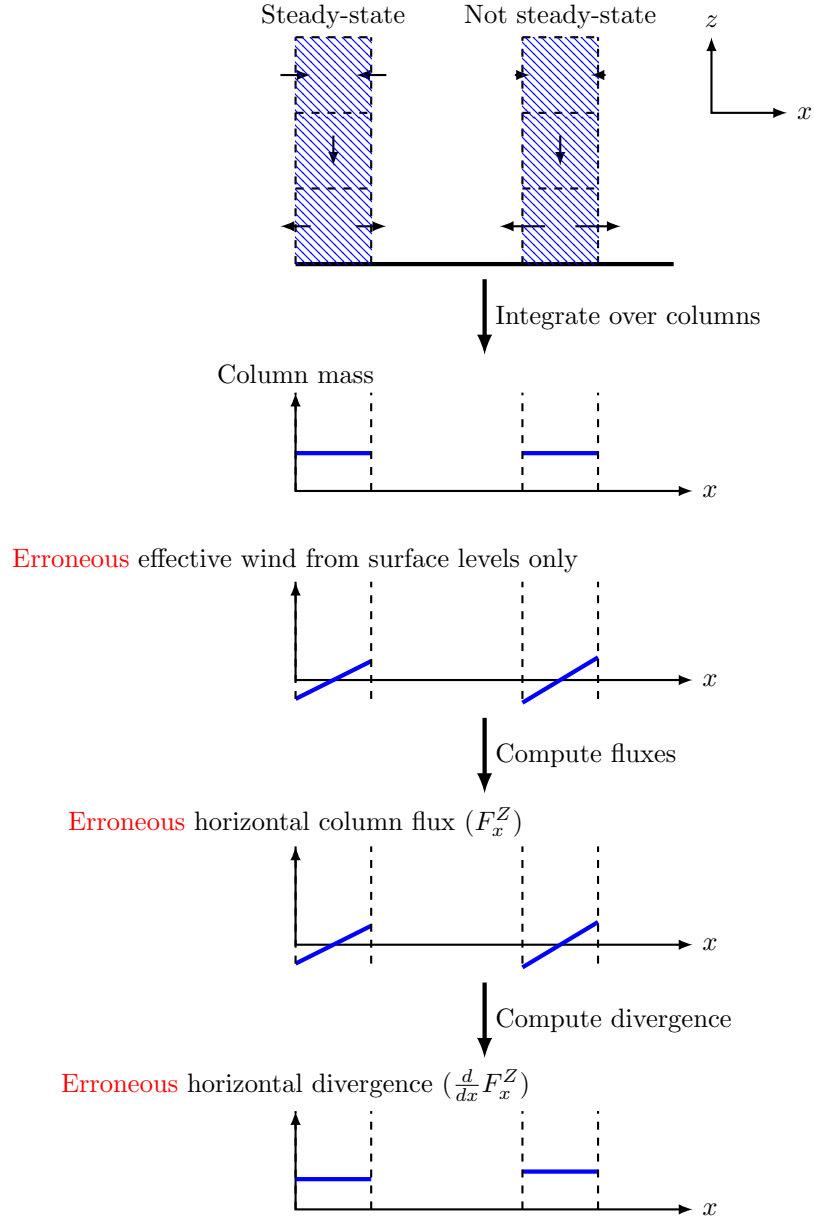
We obtain the same relation, namely, $\frac{dE_x^Z}{dx} = -\bar{E} \frac{dz_0}{dx}$. NB: in this example, we don't specify any wind flow through the valley, thus the error is not in any way proportional to F_x at the surface, contrary to what might be suggested in the derivation found in Sun (2022).

Example S7. We now consider the case of a convergent wind towards the top of the column and divergent wind towards the bottom of the column (implying vertical movement of air in-between the two regions). We consider here the case of computing the effective wind correctly.



For the steady-state column (on the left), the wind is ‘in balance’ throughout the entire column and the effective wind when integrated over the column is 0 – the rate of adding mass to the column at the top is balanced by the rate of remove mass from the column at its base. This means that the horizontal divergence is zero, in line with the fact that there is no source or sink present here. Conversely, for the non-steady-state column (on the right), the wind is not ‘in balance’ and there is effectively more outflow than inflow when averaging over the column, *at the illustrated moment*. The positive divergence term is not related to a source or sink, but to the non-steady stateness of the situation – but in applying the divergence method we assume the situation is steady-state, thus we may accidentally assume that there is a source present.

Example S8. We now consider the case of a convergent wind towards the top of the column and divergent wind towards the bottom of the column (implying vertical movement of air in-between the two regions). We now use the erroneous wind speeds, by only using as effective wind the wind speeds at the bottom of the column.



We encounter the same issue now in the steady-state and non-steady-state cases: the apparent wind divergence artificially seems to introduce ‘virtual’ sources and sinks. Such an issue would be avoided, if we would avoid computing the wind divergence term altogether, as suggested by Sun (2022).

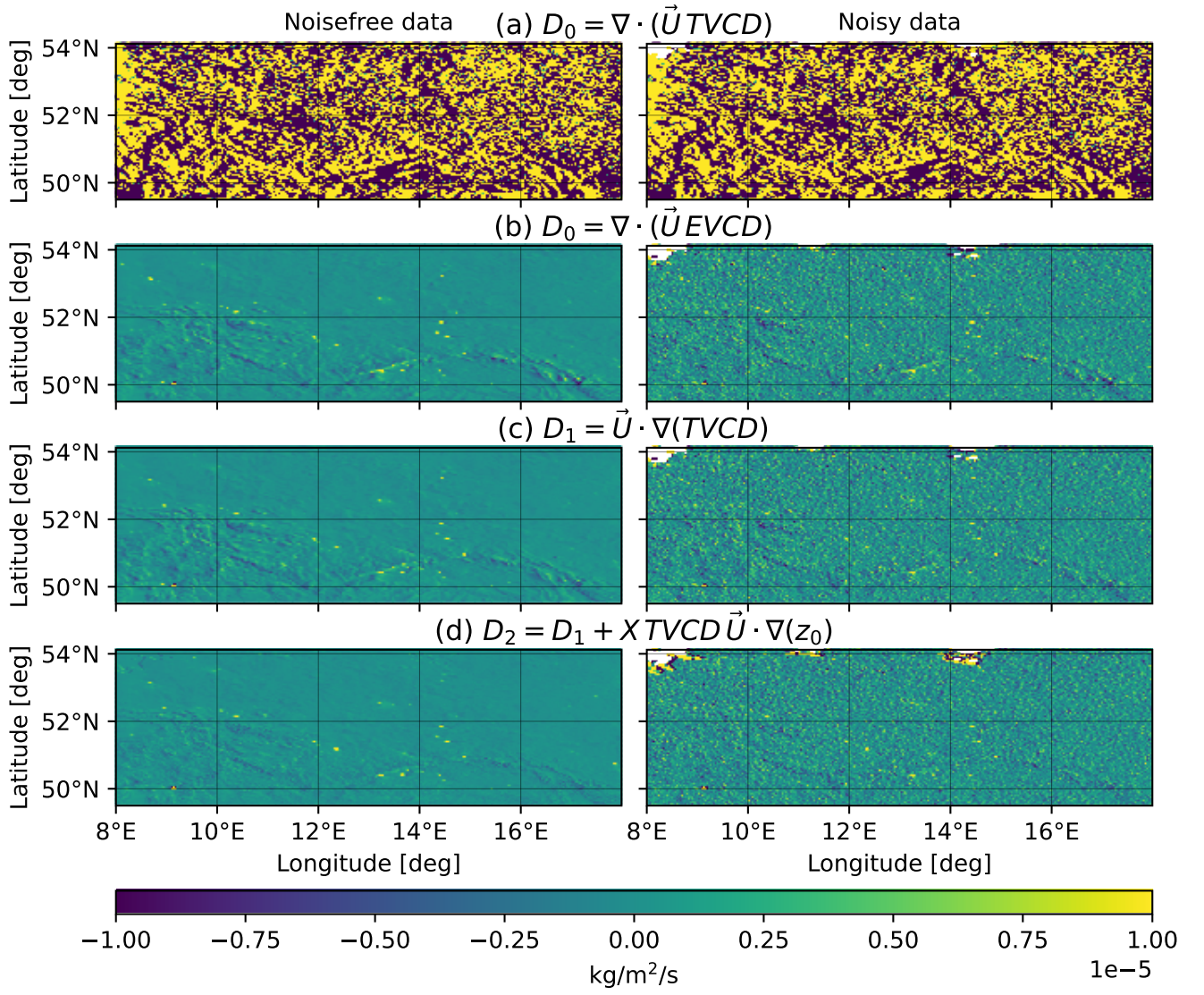


Figure S1: Four different divergence operations applied to a full year of cloudfree SMARTCARB CO₂ data, centered on the country borders of Germany, Czech Republic and Poland. The top row considers noise-free data, while the bottom row considers noisy data. The yellow dots in the figure generally correspond to point sources. The different divergence operators D_0 , D_1 and D_2 are described in the text.

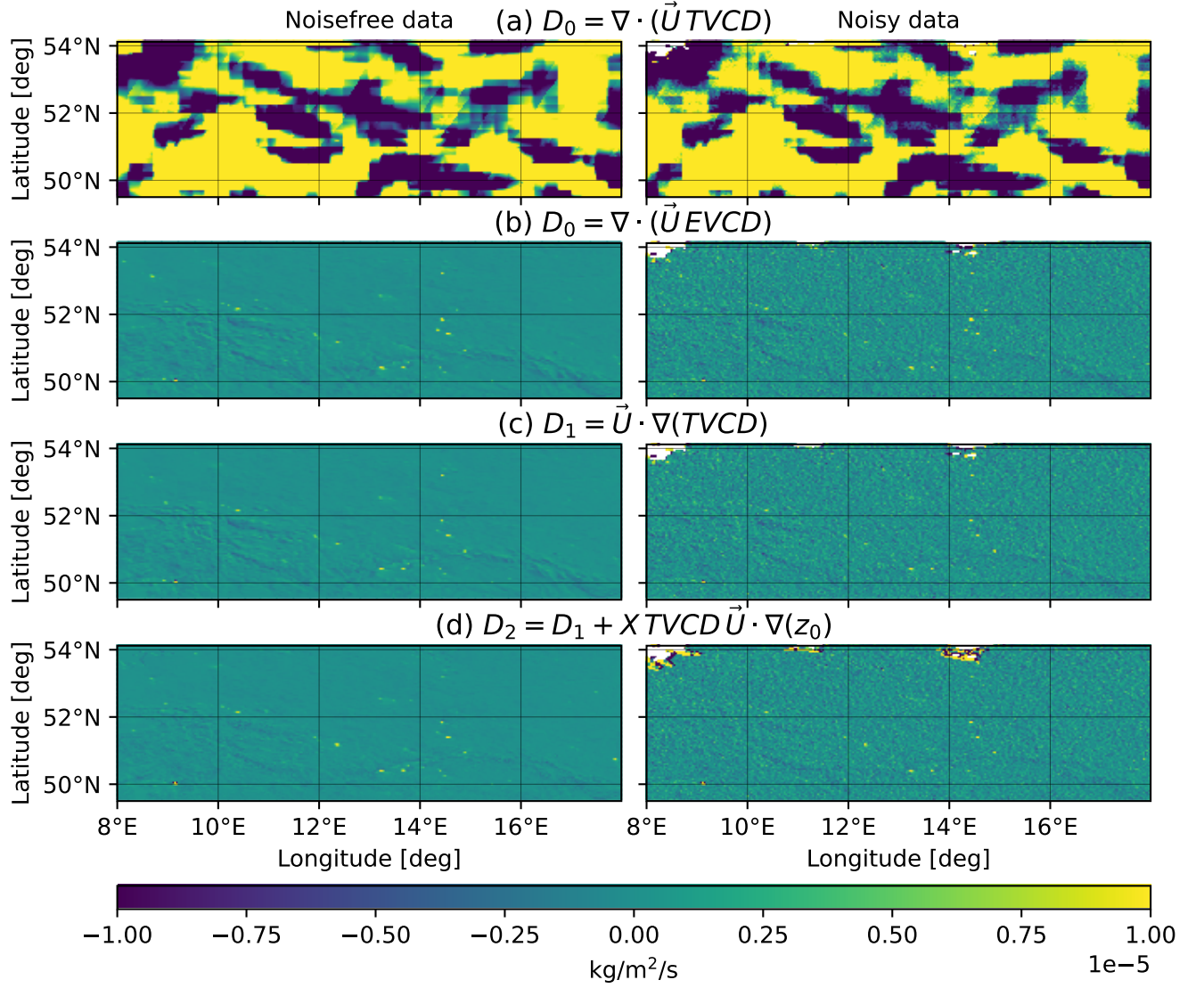


Figure S2: Four different divergence operations applied to a full year of cloudfree SMARTCARB CO₂ data, centered on the country borders of Germany, Czech Republic and Poland. The top row considers noise-free data, while the bottom row considers noisy data. The different divergence operators D_0 , D_1 and D_2 are described in the main text. The wind fields are derived from ERA-5, model level 133.

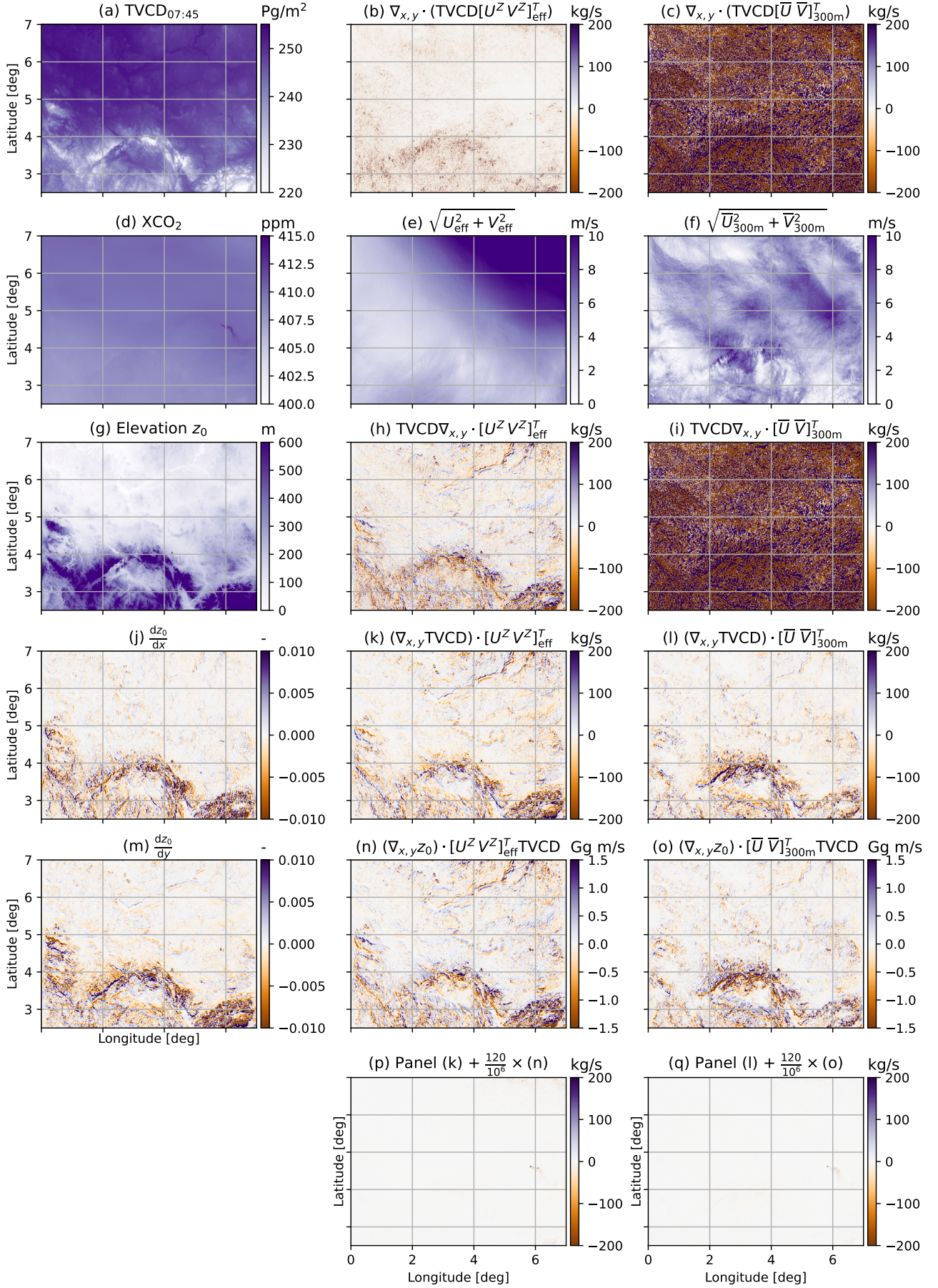


Figure S3: Panels a, d, g, j and m shows details for a simulated CO₂ TVCD with COSMO-GHG. The TVCD for CO₂ is inversely proportional to the elevation. The XCO₂ plot suppresses this topography-dependency, and reveals a strong point source. Panels b, e, h, k, n and p show various computations using the true effective wind field (i.e., concentration-weighted – some small numerical artifacts remain). Panels c, f, i, l, o and q use the wind from 50, 100, ..., 650 m altitude, shorthand called ‘300 m’. The topography correction term $\text{TVCD} [U^Z V^Z]^T \cdot \nabla_{x,y} z_0$ (shown in panels n & o) is an excellent approximation of $\text{TVCD} \nabla_{x,y} \cdot [U^Z V^Z]^T$ (shown in panel h & i; but when the erroneous wind field is used, the topography correction term gives less artifacts).

1. Derivation of the theory in spherical coordinates

When working in spherical coordinates, we consider the projection of observations onto a latitude-longitude coordinate system, e.g., with reference to the Earth's center of mass as in WGS 84.

The mass continuity equation in spherical coordinates take on a similar form as its Cartesian counterpart, but a point in space is instead described in terms of its radius r from the center of the earth, while θ and ϕ (in radians) are the latitude and longitude of the point in geographical coordinates, respectively. The coordinate $(\theta, \phi) = (0, 0)$ corresponds to the intersection between the equator and the Greenwich meridian. The continuity equation is then written as

$$\iiint_V \left(S(r, \theta, \phi, t) - \frac{\partial \rho_E(r, \theta, \phi, t)}{\partial t} \right) dV = \iiint_V \nabla \cdot \mathbf{F}(r, \theta, \phi, t; \rho_E, \mathbf{v}) dV, \quad (\text{S3})$$

where we have an elementary volume element $dV = r^2 \cos(\theta) dr d\theta d\phi$.

In spherical coordinates and under Assumption 1, we write the mass flux vector field as

$$\mathbf{F}(r, \theta, \phi, t) \equiv \rho_E(r, \theta, \phi, t) \begin{bmatrix} u(r, \theta, \phi, t) \\ v(r, \theta, \phi, t) \\ w(r, \theta, \phi, t) \end{bmatrix} = \begin{bmatrix} F_\phi(r, \theta, \phi, t) \\ F_\theta(r, \theta, \phi, t) \\ F_r(r, \theta, \phi, t) \end{bmatrix}. \quad (\text{S4})$$

The mass flux in spherical coordinates may be written as $\mathbf{F} = F_r \mathbf{r} + F_\theta \boldsymbol{\theta} + F_\phi \boldsymbol{\phi}$, using the standard spherical coordinate unit basis vectors \mathbf{r} , $\boldsymbol{\theta}$ and $\boldsymbol{\phi}$ in their respective orthogonal directions. Note that the wind field in spherical coordinates is still given in units of $[\text{m s}^{-1}]$ as in the Cartesian case.

To integrate the case of a spherical coordinate system along the z axis, we again carry out similar steps, but define the column as a volume given by the set of points satisfying $V_B = \{ (r, \theta, \phi) \mid (\theta, \phi) \in S_B, R_0 \leq r \leq R_T \}$, where S_B describes a slice through the column, and coordinate $r = R_0(\theta, \phi)$ describes the ground surface while $r = R_T(\theta, \phi)$ describes the top of the atmosphere, see Figure S4. Then we find analogously to the Cartesian case (suppressing the (r, θ, ϕ, t) dependencies momentarily for brevity) that

$$\iiint_{V_B} \nabla \cdot \mathbf{F}(r, \theta, \phi, t) dV_B = \iint_{S_B} \int_{R_0}^{R_T} \left(r \frac{\partial F_\phi}{\partial \phi} + r \frac{\partial (\cos(\theta) F_\theta)}{\partial \theta} + \cos \theta \frac{\partial (r^2 F_r)}{\partial r} \right) dr d\theta d\phi, \quad (\text{S5})$$

$$= \iint_{S_B} \left[\nabla_{\theta, \phi} \cdot \mathbf{F}^R(\theta, \phi, t) + R_0^2 \cos(\theta) \underbrace{\nabla (R_0(\theta, \phi) - r) \cdot \mathbf{F}(R_0)}_{-\mathbf{F}(R_0) \cdot \hat{\mathbf{n}}(R_0)=0} \right] d\theta d\phi, \quad (\text{S6})$$

$$= \iint_{S_B} \nabla_{\theta, \phi} \cdot \mathbf{F}^R(\theta, \phi, t) d\theta d\phi, \quad (\text{S7})$$

where we used $\mathbf{F}(R_T) \cdot \hat{\mathbf{n}}(R_T) = \mathbf{F}(R_0) \cdot \hat{\mathbf{n}}(R_0) = 0$ following Assumption 2, and define a divergence operator $\nabla_{\theta, \phi} = (\partial/\partial\phi, \partial/\partial\theta)^T$ applied to $\mathbf{F}^R = \int_{R_0}^{R_T} (r F_\phi \boldsymbol{\phi} + r \cos(\theta) F_\theta \boldsymbol{\theta}) dr = F_\phi^R \boldsymbol{\phi} + F_\theta^R \boldsymbol{\theta}$.

For the situation in spherical coordinates, we equally define an enhanced vertical column density,

$$\text{EVCD}_{S_B}(t) = \frac{\iiint_{V_B} \rho_E(r, \theta, \phi, t) dV_B}{\iint_{S_B} \cos(\theta) d\theta d\phi}, \quad (\text{S8})$$

giving a result with units of kg sr^{-1} (i.e., kilograms per steradian). Conversion from $[\text{kg/sr}]$ to $[\text{kg/m}^2]$ follows approximately through a multiplication with $R_0^2 \approx 6371000^2$, and vice versa. The fields TVCD and BG may be similarly found in spherical coordinates. Like the Cartesian case, we again formulate a density model $\rho_E = \text{EVCD}_{S_B} C_0(r, \theta, \phi, t)$, with property $\int_r C_0 r^2 dr = 1$ and $\iiint_{V_B} C_0 dV_B = \iint_{S_B} \cos(\theta) d\theta d\phi$. For example, a concentration function of the form $C_0 = \delta(R_0 + r_e - r)/r^2$ would imply that a species' enhancement is only present at a radially uniform altitude of r_e over R_0 . Using the proposed density model in eq. (S8) would indeed return the EVCD. Its use in eq. (S7) gives

$$\mathbf{F}^R(\theta, \phi, t) = \int_{R_0}^{R_T} \rho_E(r, \theta, \phi, t) \begin{bmatrix} u(r, \theta, \phi, t) r \\ v(r, \theta, \phi, t) r \cos(\theta) \end{bmatrix} dr, \quad (\text{S9})$$

$$= \text{EVCD}_{S_B}(t) \int_{R_0}^{R_T} C_0(r, \theta, \phi, t) \begin{bmatrix} u(r, \theta, \phi, t) r \\ v(r, \theta, \phi, t) r \cos(\theta) \end{bmatrix} dr, \quad (\text{S10})$$

$$= \text{EVCD}_{S_B}(t) \begin{bmatrix} U_R(\theta, \phi, t) \\ V_R(\theta, \phi, t) \end{bmatrix}, \quad (\text{S11})$$

where V_R and U_R are the winds weighed following Eq. (S10).

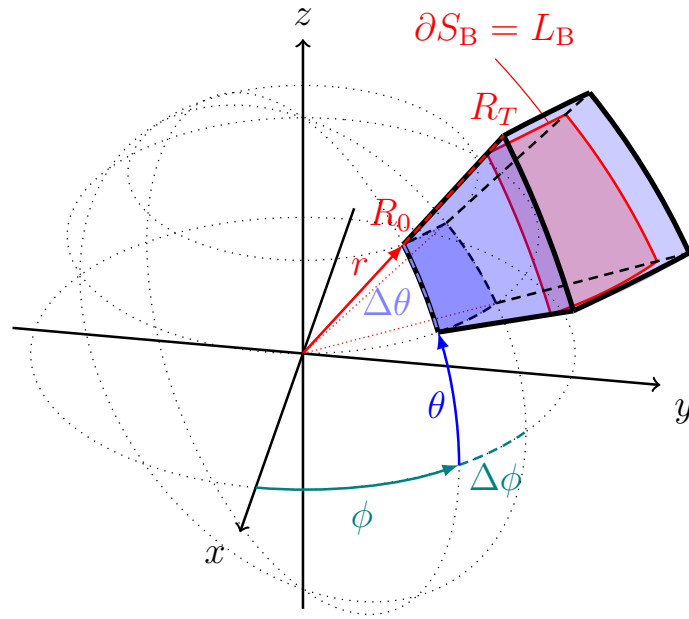


Figure S4: The integration domain V_B (in blue) consists of a spherical cone ranging from the a surface (R_0) to the top of the atmosphere (R_T). It is assumed that the normal flux (here: $\rho(r, \theta, \phi, t)w(r, \theta, \phi, t)$) vanishes at the bottom and top of this column. A slice perpendicular to the radial direction is given by the area S_B (in red), enclosed by the line $\partial S_B = L_B$.

2. Cross-sectionally integrating Gaussian plumes

In Fig. 7 it can be seen that the cross-sectional flux for a Gaussian plume computes the correct source flux Q as long as we integrate along a straight line through the entire plume; whether or not we assume the diffusive flux and whether or not the line lies perpendicular to the wind. We mathematically confirm this result in this appendix. We note that the cross-sectional flux in eq. 25 for a straight line segment from $(x_0, -y_0)$ to (x_1, y_0) for positive x locations can be written as

$$\int_{(x_0, -y_0)}^{(x_1, y_0)} \mathbf{F}^Z(x, y) \cdot (\mathbf{i} dy - \mathbf{j} dx) = \int_{-y_0}^{y_0} F_x^Z(x(y), y) dy - \int_{x_0}^{x_1} F_y^Z(x, y(x)) dx, \quad (\text{S12})$$

where we can use the line descriptions $y(x) = y_0(x_0 + x_1 - 2x)/(x_0 - x_1)$ and $x(y) = y(x_1 - x_0)/(2y_0) + (x_0 + x_1)/2$ assuming $x_0 \neq x_1$ and $y_0 \neq 0$.

The fluxes for a Gaussian plume may be written explicitly as $F_x^Z = G(x, y)U$ and $F_y^Z = G(x, y)Uy/(2x)$ for the advective and diffusive case, using $G(x, y)$ from eq. 36. The integrals in eq. (S12) may then be found. For this, we use the following two identities:

$$\frac{\partial}{\partial x} \left(\sqrt{\pi c} e^{\frac{2ab}{c}} \operatorname{erf} \left(\frac{-b - 2ax}{2\sqrt{cx}} \right) \right) = \frac{(b - 2ax)e^{-\frac{(b - 2ax)^2}{4cx}}}{2x^{3/2}}, \quad (\text{S13})$$

and

$$\frac{\partial}{\partial y} \left(\sqrt{\frac{\pi c}{2}} \left(e^{\frac{2b}{a^2 c}} \operatorname{erf} \left(\frac{ay + 2b}{a\sqrt{2c}\sqrt{ay + b}} \right) + \operatorname{erf} \left(\frac{y}{\sqrt{2c}\sqrt{ay + b}} \right) \right) \right) = \frac{e^{-\frac{y^2}{2c(ay + b)}}}{\sqrt{ay + b}}, \quad (\text{S14})$$

where erf represents the error function $\operatorname{erf}(z) = 2/\sqrt{\pi} \int_0^z e^{-t^2} dt$ and $d(\operatorname{erf}(x))/dx = \frac{2}{\sqrt{\pi}} e^{-x^2}$. They serve as useful primitive functions (i.e., anti-derivatives) for evaluating the integrals that follow.

To start with the F_y integral first,

$$\int_{x_0}^{x_1} F_y^Z(x, y(x)) dx = \int_{x_0}^{x_1} \frac{y(x)}{2x} \frac{Q}{\sqrt{2\pi}\sigma(x)} e^{-\frac{y^2(x)}{2\sigma^2(x)}} dx, \quad (\text{S15})$$

$$= \int_{x_0}^{x_1} \frac{y_0 \frac{x_0 + x_1 - 2x}{x_0 - x_1}}{2x} \frac{Q}{\sqrt{2\pi} \sqrt{\frac{2xK_y}{U}}} e^{-\frac{(y_0 \frac{x_0 + x_1 - 2x}{x_0 - x_1})^2}{4 \frac{xK_y}{U}}} dx, \quad (\text{S16})$$

$$= \frac{Q\sqrt{U}}{2\sqrt{K_y}\pi} \int_{x_0}^{x_1} \frac{y_0 \frac{x_0 + x_1 - 2x}{x_0 - x_1}}{2x^{3/2}} e^{-\frac{(y_0 \frac{x_0 + x_1 - 2x}{x_0 - x_1})^2}{4 \frac{xK_y}{U}}} dx. \quad (\text{S17})$$

We note that the integrand is the right-hand side of eq. (S13) with $a = y_0/(x_0 - x_1)$, $b = y_0(x_0 + x_1)/(x_0 - x_1)$, $c = K_y/U$. Thus, by inspection, the integral is solved as

$$\int_{x_0}^{x_1} F_y^Z(x, y(x)) dx = \frac{Q\sqrt{U}}{2\sqrt{K_y}\pi} \left(\sqrt{\pi} \sqrt{\frac{K}{U}} e^{2 \frac{y_0^2(x_0 + x_1)U}{(x_0 - x_1)^2 K_y}} \operatorname{erf} \left(\frac{y_0 \frac{-x_0 - x_1 - 2x}{x_0 - x_1}}{2\sqrt{xK_y/U}} \right) \right) \Big|_{x=x_0}^{x_1}, \quad (\text{S18})$$

$$= \frac{Q}{2} \left(e^{2 \frac{y_0^2(x_0 + x_1)U}{(x_0 - x_1)^2 K_y}} \operatorname{erf} \left(\frac{y_0 \frac{-x_0 - x_1 - 2x}{x_0 - x_1}}{\sqrt{2\sigma(x)}} \right) \right) \Big|_{x=x_0}^{x_1} (\approx 0). \quad (\text{S19})$$

When the argument of the error function approaches 2, the error function reaches its asymptotic value of 1. Thus, for a large enough value of y_0 , we will effectively subtract two identical numbers, such that eq. (S19) approaches 0.

The F_x integral can similarly be solved as

$$\int_{y_0}^{-y_0} F_x^Z(x(y), y) dy = \int_{-y_0}^{y_0} \frac{Q}{\sqrt{2\pi}\sigma(x(y))} e^{-\frac{y^2(x)}{2\sigma^2(x(y))}} dy, \quad (\text{S20})$$

$$= \int_{-y_0}^{y_0} \frac{Q}{\sqrt{2\pi} \sqrt{\frac{K_y(y/y_0(x_1 - x_0) + (x_0 + x_1))}{U}}} e^{-\frac{y^2(x)}{2 \frac{K_y(y/y_0(x_1 - x_0) + (x_0 + x_1))}{U}}} dy, \quad (\text{S21})$$

$$= \frac{Q\sqrt{U}}{\sqrt{2K_y}\pi} \int_{-y_0}^{y_0} \frac{e^{-\frac{y^2(x)}{2 \frac{K_y(y/y_0(x_1 - x_0) + (x_0 + x_1))}{U}}}}{\sqrt{(y/y_0(x_1 - x_0) + (x_0 + x_1))}} dy. \quad (\text{S22})$$

We note that the integrand is the right-hand side of eq. (S14) with $a = (x_1 - x_0)/y_0$, $b = (x_0 + x_1)$ and $c = K_y/U$. Thus, by inspection the integral is solved as

$$\int_{-y_0}^{y_0} F_x^Z(x(y), y) dy = \frac{Q}{2} \left(e^{2 \frac{y_0^2 (x_0 + x_1) U}{(x_1 - x_0)^2 K_y}} \operatorname{erf} \left(\frac{y \frac{x_1 - x_0}{y_0} + 2(x_0 + x_1)}{\frac{x_1 - x_0}{y_0} \sqrt{2\sigma(x(y))}} \right) + \operatorname{erf} \left(\frac{y}{\sqrt{2\sigma(x(y))}} \right) \right) \Big|_{y=-y_0}^{y_0}, \quad (\text{S23})$$

$$= \frac{Q}{2} \left(e^{2 \frac{y_0^2 (x_0 + x_1) U}{(x_1 - x_0)^2 K_y}} \operatorname{erf} \left(y_0 \frac{\frac{-x_0 - x_1 - 2x(y)}{x_0 - x_1}}{\sqrt{2\sigma(x(y))}} \right) + \operatorname{erf} \left(\frac{y}{\sqrt{2\sigma(x(y))}} \right) \right) \Big|_{y=-y_0}^{y_0}. \quad (\text{S24})$$

The first term in eq. (S24) is identical to eq. (S19), as $x(y_0) = x_1$ and $x(-y_0) = x_0$ at the limits. Thus, if we compute the full cross-sectional flux integral (S12) by collecting both integrals, we obtain

$$\int_{(x_0, -y_0)}^{(x_1, y_0)} \mathbf{F}_{\text{adv+dif}}^Z(x, y) \cdot (\mathbf{i} dy - \mathbf{j} dx) = \frac{Q}{2} \left(\operatorname{erf} \left(\frac{y_0}{\sqrt{2\sigma(x_0)}} \right) + \operatorname{erf} \left(\frac{y_0}{\sqrt{2\sigma(x_1)}} \right) \right) \approx Q. \quad (\text{S25})$$

When the argument of the error function approaches 2, the error function approaches its asymptotic value of 1. Hence, for a large enough y_0 , the cross-sectional flux approaches Q .

If we assume $F_y = 0$ and thus assume only advection takes place, eq. (S12) results in

$$\int_{(x_0, -y_0)}^{(x_1, y_0)} \mathbf{F}_{\text{adv}}^Z(x, y) \cdot (\mathbf{i} dy - \mathbf{j} dx) = \int_{-y_0}^{y_0} F_x^Z(x(y), y) dy \approx Q. \quad (\text{S26})$$

The approximation to Q of eq. (S26) follows identical to our comment at eq. (S19), as the subtraction of two nearly identical error functions largely cancels, provided y_0 is chosen large enough. Thus, $\int_{(x_0, -y_0)}^{(x_1, y_0)} \mathbf{F}_{\text{adv+dif}}^Z(x, y) \cdot (\mathbf{i} dy - \mathbf{j} dx) \approx \int_{(x_0, -y_0)}^{(x_1, y_0)} \mathbf{F}_{\text{adv}}^Z(x, y) \cdot (\mathbf{i} dy - \mathbf{j} dx)$.

Hence, the accuracy of the cross-sectional flux method for Gaussian plumes hardly changes, whether one chooses (a) $x_0 = x_1$ or $x_0 \neq x_1$, and/or whether one assumes (b) advection and diffusion, or merely advection, as long as one integrates over a straight line segment with large enough y offsets.

References

- Brunner, D., Kuhlmann, G., Marshall, J., Clément, V., Fuhrer, O., Broquet, G., ... Meijer, Y. (2019). Accounting for the vertical distribution of emissions in atmospheric CO₂ simulations. *Atmospheric Chemistry and Physics*, 19(7), 4541–4559.
- Kuhlmann, G., Clément, V., Marshall, J., Fuhrer, O., Broquet, G., Schnadt-Poberaj, C., ... Brunner, D. (2020). *Synthetic XCO₂, CO and NO₂ observations for the CO₂m and sentinel-5 satellites*. Zenodo. Retrieved 2023-12-21, from <https://zenodo.org/records/4048228> doi: 10.5281/zenodo.4048228
- Sun, K. (2022). Derivation of emissions from satellite-observed column amounts and its application to TROPOMI NO₂ and CO observations. *Geophysical Research Letters*, 49(23), e2022GL101102.